AGU PUBLICATIONS

JGR

Journal of Geophysical Research: Space Physics

RESEARCH ARTICLE

10.1002/2017JA024187

Key Points:

- Slightly southward, on average, fluctuating IMF B_z drives higher nightside ULF range-integrated magnetic power spectral densities
- Slightly southward, on average, fluctuating IMF B_z drives enhanced whistler mode chorus wave activity in the outer Van Allen belt
- Substorm-injected electrons, large-amplitude ULF fluctuations, and enhanced chorus wave power are important for outer belt electron flux recovery

Correspondence to:
V. M. Souza,
vitor.souza@inpe.br

Citation:
Souza, V. M., et al. (2017), Acceleration of radiation belt electrons and the role of the average interplanetary magnetic field B_z component in high-speed streams, *J. Geophys. Res. Space Physics*, *122*, 10,084–10,101, doi:10.1002/2017JA024187.

Received 24 MAR 2017
Accepted 7 AUG 2017
Accepted article online 10 AUG 2017
Published online 17 OCT 2017

Acceleration of radiation belt electrons and the role of the average interplanetary magnetic field B_z component in high-speed streams

V. M. Souza[1], R. E. Lopez[2], P. R. Jauer[1], D. G. Sibeck[3], K. Pham[4], L. A. Da Silva[1], J. P. Marchezi[1], L. R. Alves[1], D. Koga[1], C. Medeiros[1], M. Rockenbach[1], and W. D. Gonzalez[1]

[1]National Institute for Space Research/INPE, São Paulo, Brazil, [2]Department of Physics, University of Texas at Arlington, Arlington, Texas, USA, [3]NASA/Goddard Space Flight Center, Greenbelt, Maryland, USA, [4]Department of Physics and Astronomy, West Virginia University, Morgantown, West Virginia, USA

Abstract In this study we examine the recovery of relativistic radiation belt electrons on 15–16 November 2014, after a previous reduction in the electron flux resulting from the passage of a corotating interaction region (CIR). Following the CIR, there was a period of high-speed streams characterized by large, nonlinear fluctuations in the interplanetary magnetic field (IMF) components. However, the outer radiation belt electron flux remained at a low level for several days before it increased in two major steps. The first increase is associated with the IMF background field turning from slightly northward on average to slightly southward on average. The second major increase is associated with an increase in the solar wind velocity during a period of southward average IMF background field. We present evidence that when the IMF B_z is negative on average, the whistler mode chorus wave power is enhanced in the outer radiation belt, and the amplification of magnetic integrated power spectral density in the ULF frequency range, in the nightside magnetosphere, is more efficient as compared to cases in which the mean IMF B_z is positive. Preliminary analysis of the time evolution of phase space density radial profiles did not provide conclusive evidence on which electron acceleration mechanism is the dominant. We argue that the acceleration of radiation belt electrons requires (i) a seed population of keV electrons injected into the inner magnetosphere by substorms and both (ii) enhanced whistler mode chorus waves activity as well as (iii) large-amplitude MHD waves.

1. Introduction

The outer Van Allen belt is in part composed of trapped electrons with relativistic ($\gtrsim$1 MeV) energies. These electrons pose a major threat to spacecraft at and below geosynchronous orbits since they can cause both structural damages and degradation of spacecraft components [*Wrenn and Smith*, 1996]. Furthermore, relativistic electron precipitation impacts the chemical composition and possibly the dynamics of the outermost layers of the Earth's atmosphere [*Horne et al.*, 2009]. Therefore, it is of the utmost importance to monitor the variations of outer belt electron fluxes.

Although not fully understood yet, variations in the outer belt electron fluxes have been shown to be strongly correlated with the interplanetary medium activity, particularly to the occurrence of high-speed solar wind streams (HSS) [*Blake et al.*, 1997; *Baker et al.*, 1997; *Meredith et al.*, 2011; *Miyoshi et al.*, 2013] and interplanetary coronal mass ejections (CMEs) [*Reeves et al.*, 1998; *Baker et al.*, 1998; *Kataoka and Miyoshi*, 2006; *Hietala et al.*, 2014; *Kilpua et al.*, 2015].

Trying to investigate the entire radiation belt response to different solar wind drivers, *Reeves et al.* [2003] gathered 276 geomagnetic storms which usually follow the arrival of either HSS or CMEs and found that in about 50% of the cases there was an increase in the flux of relativistic electrons, while in about 25% there was a decrease, and in the other 25% no appreciable changes occurred. *Reeves et al.* [2003] attributed the observed changes in relativistic electron fluxes to a delicate balance between the acceleration and loss processes occurring in the inner magnetosphere. *Hietala et al.* [2014] and *Kilpua et al.* [2015], on the other hand, have more recently focused on the interplanetary causes for relativistic electron flux variations. *Hietala et al.* [2014] showed that higher ultralow frequency (ULF) power in magnetic field and dynamic pressure fluctuations in the CME's sheath region are associated with strong electron depletions at geosynchronous orbit. *Kilpua et al.* [2015] investigated the overall radiation belt response, i.e., depletion, enhancement, and no change, to solar wind substructures like CME's ejecta and sheath and slow-fast stream interaction regions. They have found that electron flux enhancements occur during fast solar wind streams trailing the stream interface or the CME, while electron flux depletions occur during stream interface regions, CME ejecta, and sheaths.

The influence of the southward versus northward interplanetary magnetic field (IMF) B_z component within HSS events on the control of the electron flux in the radiation belts was analyzed, among others, by *Miyoshi and Kataoka* [2008] and *Miyoshi et al.* [2013]. By performing a superposed epoch analysis, *Miyoshi and Kataoka* [2008] showed that southward IMF-dominant HSS controls electron flux enhancements at geosynchronous orbit in stream interaction region events. They have also found that northward IMF-dominant HSS was associated with lesser outer belt electron flux enhancements as opposed to southward IMF-dominant HSS. More recently, *Miyoshi et al.* [2013] have shown that during southward IMF-dominant HSS the chorus wave activity is increased in the inner magnetosphere, which in turn would be responsible for accelerating electrons up to relativistic energies. Somewhat akin to what *Miyoshi and Kataoka* [2008] have found, *Miyoshi et al.* [2013] noticed that for northward IMF-dominant HSS periods the chorus wave activity is not as intense, and therefore, the chorus acceleration mechanism is not effective during these periods, which ends up with a lesser or no appreciable change in the outer belt electron flux. Corroborating this analysis, we recall that according to *Tsurutani et al.* [2006, and references therein], chorus waves are generated by the loss cone instability of electrons in the 5–40 keV energy range injected in the nightside magnetosphere during substorms, which in turn has its occurrence intensified during southward IMF-dominant HSS events.

Inside HSS, one often finds Alfvénic magnetic field fluctuations that may or may not have large amplitudes, i.e., $\delta B/B \gtrsim 1$, where δB is the peak-to-peak wave amplitude and B the local magnetic field magnitude [*Tsurutani et al.*, 2006]. These waves can produce a significant amount of southward IMF B_z field [see *Gonzalez et al.*, 2006], which allows dayside magnetopause reconnection to take place, and therefore drive an intense magnetospheric convection and substorm activity. Substorm-injected electrons in the keV energy range can then function as a seed population [see, e.g., *Kim et al.*, 2000] for a number of electromagnetic waves that can resonantly interact with these electrons and accelerating them up to MeV energies. Either low-frequency waves (in a few to tens of mHz range) like ULF waves [*Rostoker et al.*, 1998; *Elkington et al.*, 1999; *O'Brien et al.*, 2003] or higher-frequency waves in the hundreds to thousands of hertz range like whistler mode chorus waves [*Horne et al.*, 2003a, 2003b; *Thorne et al.*, 2013] can participate in such interactions.

In this work we analyze the outer belt relativistic electron flux variations that took place on November 2014, in particular the outer belt recovery that started on around the midday of 15 November just some hours after the fluctuating IMF B_z component turned from an on average northward to an on average southward orientation. We attempt to establish the likely causes for the electrons being accelerated up to the MeV energy range and consequently refill the outer radiation belt. We focus on the role played by the fluctuating IMF, specifically the average (baseline) southward IMF B_z component, and the observed effects on the outer radiation belts. As tools for supporting our analysis we use the *AE* index, in situ spacecraft observations covering the near midnight to dawn sectors of the inner magnetosphere, results from a simulation of the event using the Lyon-Fedder-Mobarry (LFM) code [*Lyon et al.*, 2004], and a set of simplified physics runs of the magnetospheric environment using the 3-D global Block-Adaptive-Tree Solarwind Roe Upwind-Scheme (BATS-R-US) code [*Tóth et al.*, 2012]. It is argued that the observed electron acceleration requires both a seed population provided by nightside, hot (10's to 100's of keV energy) electron injections due to substorm activity and the presence of both large-amplitude ULF range waves and an enhanced whistler mode chorus waves activity. In particular, our global (magnetohydrodynamic - MHD) simulations show that under slightly (on average) southward IMF B_z driving the integrated magnetic power spectrum density in the ULF waves range, at and beyond the geosynchronous orbit in the nightside region, is higher as compared to those under slightly (on average) northward IMF B_z; thus, wave-particle interactions mediated by both electromagnetic waves in the ULF and chorus frequency ranges are a plausible mechanism for accelerating the observed electrons up to MeV energies.

2. Data Set

In this study, the outer radiation belt electron flux variations in the 1.8 up to 4.2 MeV energy range were acquired at spin time resolution (∼ 11 s) by the Relativistic Electron-Proton Telescope (REPT) [*Baker et al.*, 2013]

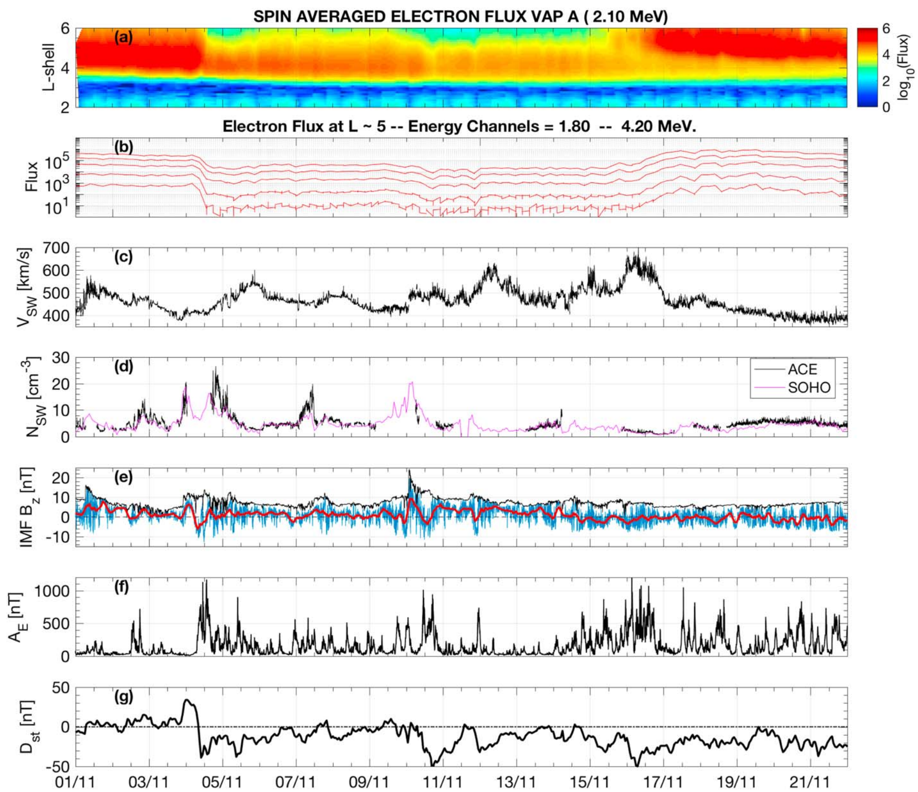

Figure 1. Radiation belts, solar wind, and geomagnetic indexes data during 1–22 November 2014. (a, b) The energetic electron flux data in units of (particles/(cm^2 s sr MeV)) from the REPT instrument on board the Van Allen Probe A satellite. (c–e) Interplanetary medium data as acquired by both ACE and SOHO spacecraft. ACE's solar wind speed and proton density at ~1 min time resolution are shown in Figures 1c and 1d, respectively, and 16 s time resolution data of the IMF magnitude (black), the IMF B_z (blue), and the IMF B_z baseline (red) calculated from a 4 h running average are shown in Figure 1e. ACE's solar wind density gaps are filled by SOHO's hourly averaged ion density data in Figure 1d. (f, g) The *AE* and *Dst* indexes, respectively.

instrument on board the Van Allen Probe A [*Mauk et al.*, 2013], while electron flux variations at lower energies were obtained by the Magnetic Electron Ion Spectrometer (MagEIS) instrument [*Blake et al.*, 2013] also onboard Van Allen Probe A. Magnetic field data from the Van Allen Probes was provided by the Electric and Magnetic Field Instrument Suite and Integrated Science (EMFISIS) instrument [*Kletzing et al.*, 2013]. Magnetic field and plasma data at the near local midnight magnetosphere region were provided by the three Time History of Events and Macroscale Interactions during Substorms (THEMIS) [*Angelopoulos et al.*, 2008] spacecraft, namely, THEMIS A, D, and E. THEMIS A spin resolution (~ 3 s) magnetic field, ion moments, and energetic (i.e., $E \gtrsim 30$ keV) electron fluxes data were obtained, respectively, by the Flux Gate Magnetometer [*Auster et al.*, 2009], the ion electrostatic analyzer [*McFadden et al.*, 2009], and the Solid State Telescope (SST) instruments. Unless otherwise stated, all vector quantities are presented in the geocentric solar magnetospheric (GSM) coordinate system.

3. Radiation Belts Overview and Solar Wind Conditions

Figure 1 presents an overview of the interplanetary medium and Earth's radiation belts conditions on 1–22 November 2014 period. Figures 1a and 1b show Van Allen Probe A's relativistic electron data, whereas Figures 1c–1e present solar wind and 1f and 1g geomagnetic indices *AE* and *Dst* data. The ACE data are plotted at the L1 position, so they must be lagged by 50 min (on average) to be compared with data at Earth. Early on 4 November a sudden compression on the magnetosphere was followed by a period of southward IMF that resulted in a *Dst* response of about 40 nT. By midday on 4 November Van Allen Probe A recorded a substantial reduction ($\gtrsim$1 order of magnitude) of the relativistic electron flux at and above $L = 5$, where L stands for the equatorial location in Earth radius of a set of dipole-like magnetic field lines [*McIlwain*, 1961]. The flux at $L \gtrsim 5$ remained low for many days after that until the middle of 15 November.

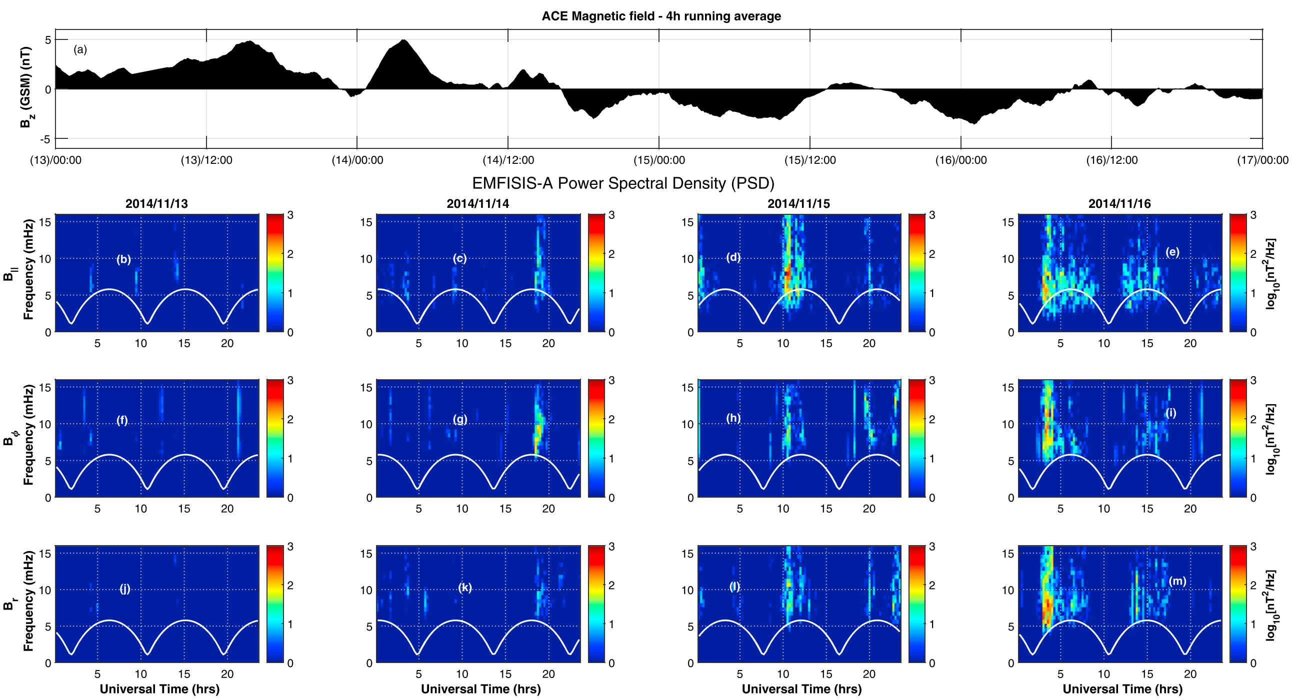

Figure 2. Power spectral density (PSD) analysis from EMFISIS's fluxgate magnetometer data onboard Van Allen Probe A for the 13–17 November 2014 period. (a) The IMF B_z baseline (4 h running average). The filled (black) region highlights the times when the baseline was either positive or negative. (b–m) PSDs in the ULF Pc4–5 frequency range for magnetic field components in the mean field-aligned coordinate system. The Van Allen Probe A radial position, in Earth radii, relative to Earth's center is overplotted as a white line in Figures 2(b–m) The value of the radial position can be also viewed on the left vertical axis of these panels.

From 4 November to 18 November, one can see in Figures 1c–1e that while the baseline values for the IMF B_z magnetic field component were not particularly large except for relatively brief periods such as the start of 10 November, the magnetosphere never reached to the "saturated" state, where there is a nonlinear dependence between the cross polar cap potential and the interplanetary electric field, $\mathbf{V}_{sw} \times \mathbf{B}_{IMF}$ (where $\mathbf{V}_{sw}$ is the solar wind velocity) since the solar wind was never in a low Mach number state [see, e.g., *Lopez et al.*, 2010]. The level of fluctuation activity in this period was large with $\delta B_z/B_z > 1$, as one would expect in high-speed streams [see *Tsurutani et al.*, 2006, and references therein]. We notice that a similar behavior for the other two magnetic field components, i.e., IMF B_x and B_y (not shown) can be seen.

The recovery of the outer belt electron flux began on 15 November and intensified on 16 November. Figures 1a and 1b show that the major refilling of the outer belt occurred midday on the 15th and also in the later morning hours of the 16th. What can be seen from Figures 1c and 1f is that the solar wind speed and *AE* activity both picked up on the 15th, especially around midday. On the 16th, *AE* activity became very intense reaching values as high as 1000 nT as the solar wind speed plateaued above 600 km/s. This was the period when the MeV electron flux recovered to its prestorm level, at least at $L = 5$. Figures 2 and 3 show power spectral density (PSD) analysis of magnetometer data on board the Van Allen Probe A during the 13–17 November period. Waves in both the ULF Pc4–5 frequency range (Figure 2) and whistler mode chorus frequency range (Figure 3) are shown. One can see that Van Allen Probe A detection of enhanced ULF and chorus waves activity roughly coincided with the southward turning of the average (baseline) IMF B_z component (top panel in both figures) which took place around 16:00 UT on the 14th. Before that, minor or nearly absent wave activity was measured by the magnetometers aboard Van Allen Probe A whose orbit was covering the dawn flank magnetosphere. As the IMF B_z baseline turned southward, and the solar wind speed increased from ~500 to ~600 km/s in the 15–16 November period, both ULF and chorus wave activities increased substantially and persisted for many Van Allen Probe A orbits. The magnetic power spectral density values observed during the bursts of intensified chorus waves activity were in the 10^{-6}–10^{-3} nT^2/Hz range, which seems to be enough to accelerate hundreds of keV energy electrons up to MeV energies [e.g., *Horne et al.*, 2003b; *Li et al.*, 2014]. As for the ULF wave power, we note that the peak values for the compressional ($B_{||}$) mode found here, of about 10^3 nT^2/Hz in 15 November onward, were between 6 and 7 mHz, and they were somewhat close to those

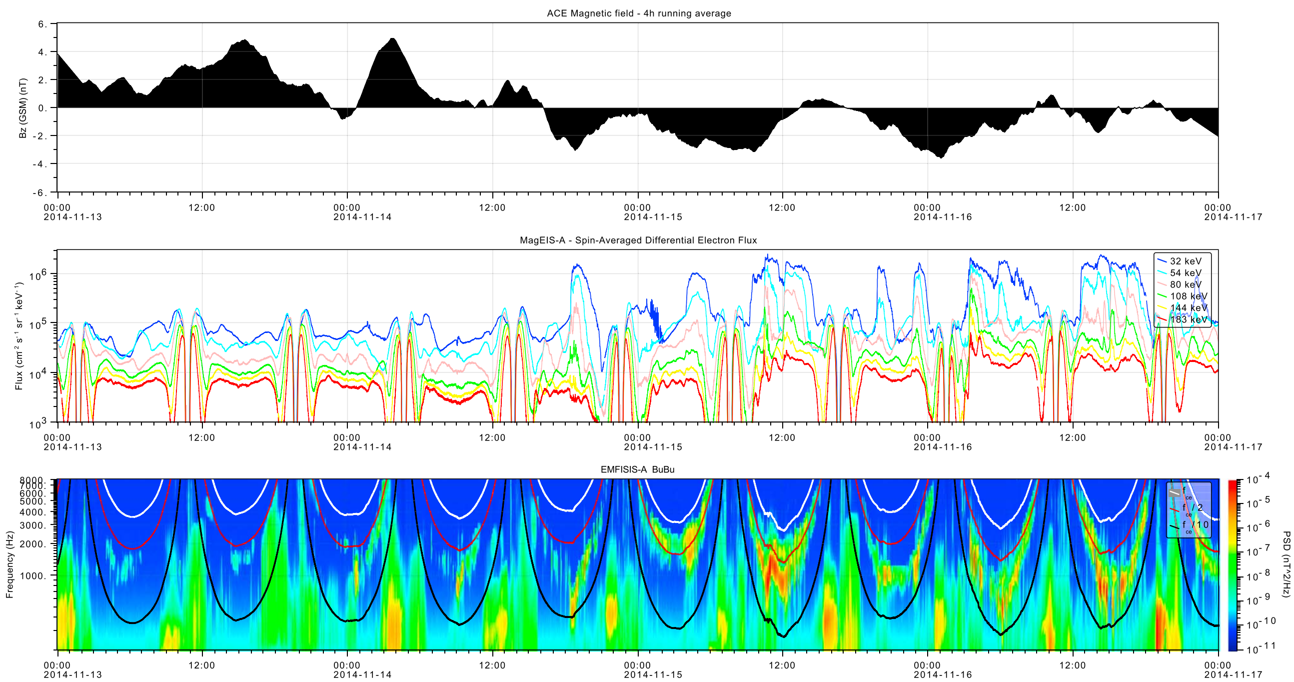

Figure 3. IMF B_z baseline, electron injections, and power spectral density (PSD) analysis from EMFISIS's fluxgate magnetometer data onboard Van Allen Probe A for the 13–17 November 2014 period. (top) The IMF B_z baseline (4 h running average). The filled (black) region highlights the times when the baseline was either positive or negative. (middle) Lower energy (tens to low hundreds of keV) electron fluxes from the MagEIS instrument. (bottom) PSD in the whistler mode chorus waves frequency range for one of the magnetic field components in the spacecraft spin plane. White, red, and black curves correspond to f_{ce} (the electron cyclotron frequency) $f_{ce}/2$, and $f_{ce}/10$, respectively.

found by *Jaynes et al.* [2015] ($\sim 10^{3.5}$ nT^2/Hz in their Figure 9) at a similar (5–6 mHz) frequency range. In their study, where they analyze a several days period of low levels of relativistic electron fluxes preceded by a flux dropout, *Jaynes et al.* [2015] argued that ULF waves could be playing a direct role on the outward transport of electrons, thus contributing to their escape from the outer radiation belt. Here though, ULF waves can be contributing to inward diffuse electrons thereby increasing their energy.

4. Substorm Injections During the Outer Belt Recovery: THEMIS Observations and MHD (LFM) Simulation

Higher *AE* activity is an indicative of particle injections in the nightside magnetosphere, and these particles can function as seed populations for either cyclotron or drift resonant wave-particle interactions. Fortunately, the three THEMIS spacecraft, namely, THEMIS A (ThA), THEMIS D (ThD), and THEMIS E (ThE), were located in the nightside inner magnetosphere with their orbit's apogee in the 22–23 local time (LT) range, as shown in Figure 4, so we could verify whether substorm injections were occurring during the recovery phase of the outer radiation belt. Figure 5 shows three sets of one daylong ThA magnetic field and plasma data plots for 14 November (a–d), 15 (e–h), and 16 (i–l), for the year 2014. Each set of four panels shows, from top to bottom, magnetic and ion velocity fields in the GSM coordinate system, ion density, and hot ($E \gtrsim 25$ keV) electron flux data from the SST instrument. The other two THEMIS spacecraft presented similar signatures to those that will be discussed below.

Two things are evident from Figure 5. First, substorm activity (i.e., particle injections from the magnetotail) seen by ThA was much stronger on 15 and 16 November as compared to 14 November. This is consistent with Figure 1 that shows *AE* activity picking up at the end of 14 November, becoming larger and fairly continuous the next day, then intensifying even further on 16 November. The daily average IMF $\delta B_z = \overline{|B_z - B_z^{\text{4h running average}}|}$ (not shown), where the overbar means arithmetic mean over 1 day period, was not very different between the three days (2.12 nT, 1.64 nT, and 2.29 nT). However, the IMF was mostly northward on 14 November (until the end of the day) as it can be seen in Figure 1e, whereas it was generally southward on 15 and 16 November. Because the fluctuations were large, there were plenty of times when the IMF at the

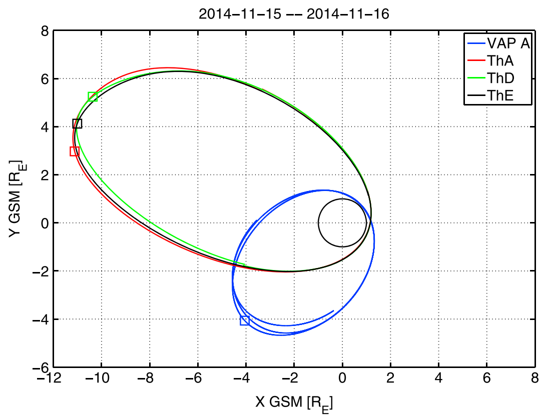

Figure 4. Van Allen Probe A and three THEMIS (ThA, ThD, and ThE) spacecraft orbits in the *XY* GSM plane for the 15–16 November 2014 period. The Van Allen Probes have a ∼ 9 h orbital period, and as a result approximately three orbits are shown for a 1 day period, while THEMIS's orbital period is approximately 24 h. The squares mark the location of each spacecraft at 12:00 UT on 15 November.

Earth was southward on 14 November, but not in a sustained fashion until the end of the day, after ∼16:00 UT. Second, if we examine the flow bursts and corresponding injections and dipolarizations [*Runov et al.*, 2009], the pattern seems to be not only that the intensity of substorm activity increases over the 3 days but also that the location of activity seems to move closer to Earth. For example, the major dipolarization (bursty bulk flow) on 14 November occur well beyond 10 R_E, just before 12:00 UT and around 13:30 UT. But on 15 November there was a dipolarization event at ∼8 R_E just before 04:00 UT, as well as one at ∼9.3 R_E at 16:00 UT. On 16 November there were several dipolarization events in the 7.5–9.5 R_E range, such as those in the early hours of the day. Moreover, the overall flux levels of keV electrons were much higher on 16 November compared to 14 November. These observations suggest that over the course of the 3 days, not only was substorm activity more intense but it also penetrated deeper into the inner magnetosphere, which began to build up a flux of keV electrons that are the seed population for further acceleration to MeV energies.

THEMIS data are single point observations, and we would like to have a global sense of magnetotail activity during these days. The Lyon-Fedder-Mobarry (LFM) code [*Lyon et al.*, 2004] has been used to successfully simulate substorms for a number of events [e.g., *Lopez et al.*, 1998; *Papadopoulos et al.*, 1999; *Wiltberger et al.*, 2000], as well as simulating the magnetospheric response to high-speed streams such as the ones being considered here [*Wiltberger et al.*, 2012; *Lopez et al.*, 2012]. The magnetospheric response to the solar wind was simulated from 13 to 16 November 2014 using the ACE data as input. Where 1 min data were not available, the available data were linearly interpolated to 1 min values. The data were then ballistically propagated to the LFM simulation grid where averaging or interpolation was used to produce a continuous 1 min solar wind time series. The LFM codes uses solar magnetic coordinates wherein the *z* axis is chosen parallel to the Earth's magnetic dipole being positive toward the Northern Hemisphere, and the *y* axis is perpendicular to the Sun-Earth line being positive toward dusk. The *x* axis completes the right-handed system. The *x* component of the IMF was set to zero throughout the simulation. LFM incorporates the *x* component of the IMF by expressing it as a linear function of the other two components in order to maintain a divergence free field. However, for long-duration runs, the fit is generally not a good one over the entire period, so the *x* component of the IMF is often just set to zero [e.g., *Wiltberger et al.*, 2012]. The resulting time series was fed into LFM as the solar wind boundary condition. The ionospheric boundary condition was set by the semiempirical conductivity model [*Lyon et al.*, 2004] with the $F_{10.7}$ flux set at 158 (the average value for the four days).

The LFM simulation of the event provides us with a global overview of the evolution of the magnetosphere over the period in question. In Figure 6 one can see three different days sets of flow channels (colored vectors) in the equatorial plane produced by the simulation. These flow channels are seen in the LFM simulation during periods of reconnection in the tail during storm and substorm simulations [e.g., *Papadopoulos et al.*, 1999; *Wiltberger et al.*, 2000]. Their properties have a strong resemblance (high speed, low density) to those of Bursty Bulk Flows [*Angelopoulos et al.*, 1992]. They are produced as low entropy flux tubes and created near the reconnection regions in the tail, which then move earthward. The source locations of the flows tend to be closer to Earth for larger southward IMF [*Lopez et al.*, 2009], and during continuous activity in the LFM code new tail reconnection sites tend to appear closer to the Earth over time if the model is continuously driven by southward IMF.

The general correspondence between activity in the simulation (notably flow bursts in the magnetotail) and *AE* activity is generally good. During periods where *AE* was low, such as throughout the 13th, there is essentially no activity in the magnetotail (not shown). When *AE* activity intensifies, there is considerable activity

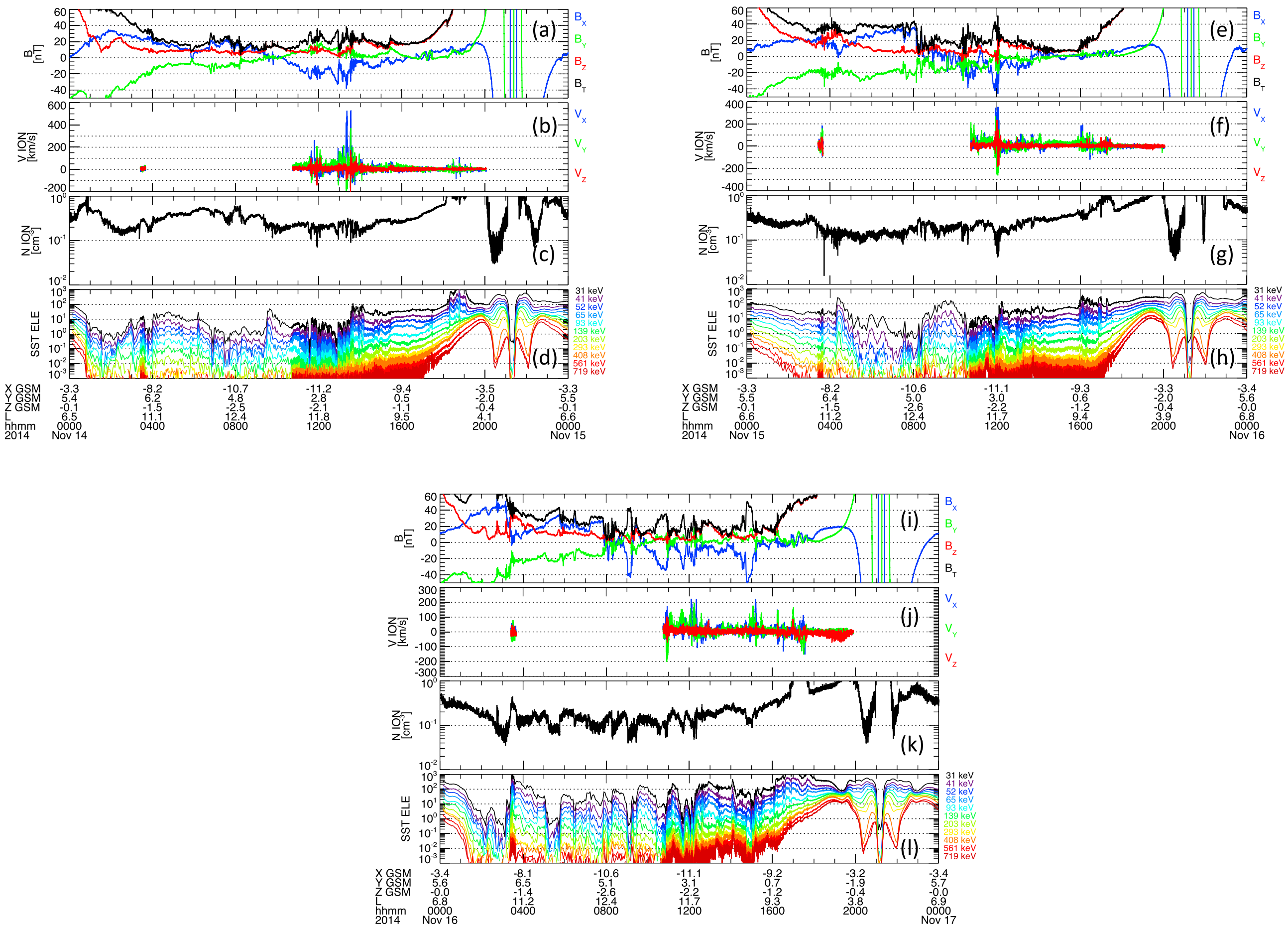

Figure 5. THEMIS A (ThA) magnetic field and plasma data during a 1 day period on (a–d) 14, (e–h) 15, and (i–l) 16 November 2014. Each set of four panels shows, from top to bottom, magnetic field and ion velocities in the GSM coordinate system, ion density, and the SST electron flux. Gaps in the velocity data refer to times when there was no ∼ 3 s resolution data available, and SST electron flux during these periods is shown in a ∼ 5 min time resolution.

in the tail. Three examples are presented in Figure 6, one each from 14, 15, and 16 November. Figure 6 (top) (14 November 18:31 UT) was during a period where *AE* had risen sharply to over 500 nT, and it shows several high-speed flow channels in the tail. Figure 6 (middle) (15 November 08:45 UT) is about the time that *AE* shows a sudden spike to 700 nT, while Figure 6 (bottom) (16 November 08:54 UT) is in the middle of ongoing activity that had *AE* excursions up to 1000 nT. All three periods show the high-speed flow channels that are characteristic of substorm and storm activity in the magnetotail. Such flow channels are characterized in our simulations by reddish and darker vectors, at all three panels, presenting finger-like structures which are more than 600 km/s plasma flows. It can be seen that activity seems to be getting closer to the Earth as the time progresses, just as the THEMIS data suggested.

The earthward head of each flow channel can be identified by a sudden reduction of velocity, with the plasma velocity quite often curling around and sometimes turning tailward, suggesting a rebound effect due to the pileup of the magnetic field at the head of the flow burst [*Lopez et al.*, 1994]. On 14 November the earthward heads of these channels (going from postmidnight at the top to premidnight at the bottom) penetrated to a radial distance of 9.1 R_E, 11.6 R_E, and 11.0 R_E, respectively, although the closest flow channel was out on the flank and seemed to be the weakest of the three. On 15 November the head of the flow channel in the early postmidnight sector penetrated to 9.0 R_E, whereas on 16 November the flow channel near midnight penetrated to 8.8 R_E. In general, what can be seen is that as the time proceeded from 14 to 15 November and then to 16, the simulation developed more intense activity in the tail, with the flow bursts penetrating

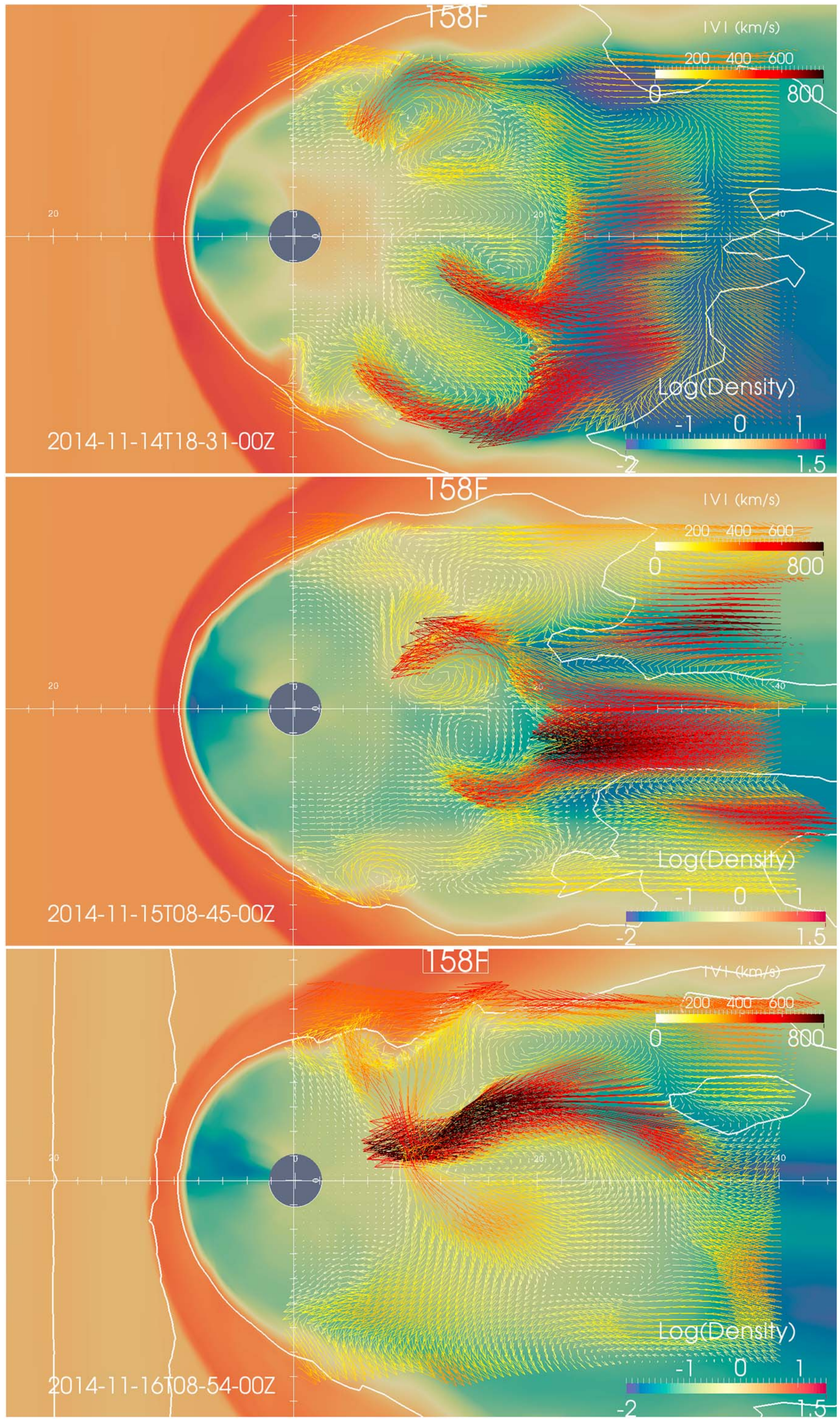

Figure 6. Results from the LFM simulation of the event showing the state of the magnetotail at three times, on (top) 14, (middle) 15, and (bottom) 16 November 2014. The views are of the equatorial plane, and the tick marks are at 2 R_E intervals. The grey circle at the origin is the inner boundary of the MHD magnetosphere simulation. The Log(Density) is color coded. The plasma velocity is indicated by the scaled arrows, which are also color coded. The white line indicates a $B_z = 0$ contour.

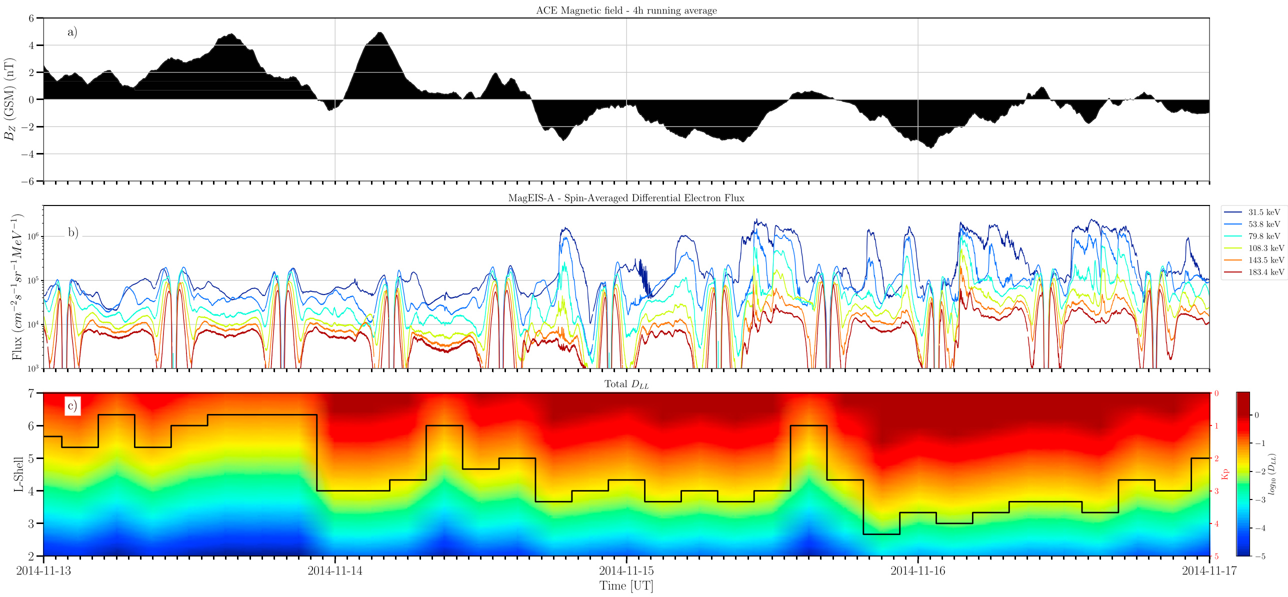

Figure 7. A 4 day period starting from 13 November 2014 showing (a) the IMF B_z baseline (4 h running average) with the filled (black) region highlighting the times when the baseline was either positive or negative, (b) lower energy (tens to low hundreds of keV) electron fluxes from the MagEIS-A instrument, and (c) the empirical, *Kp* index-based radial diffusion coefficient D_{LL} from *Ozeke et al.* [2014]. The black trace overplotted in this panel is the *Kp* index value for the period shown.

deeper into the inner magnetosphere, especially near midnight. Since the solar wind driver (in the sense of the running average of the IMF) becomes more stronger and consistently southward from the 14th to the 16th this is consistent with the THEMIS observations in Figure 5, as well as with the development of *AE* over the 3 days.

Finally, we can examine the Van Allen Probe data directly to compare with the scenario that emerges from the THEMIS data and the LFM simulation. Figure 7a shows the 4 h running average IMF B_z data, Figure 7b the electron flux data in the tens to low hundreds of keV energy range as obtained from the MagEIS instrument onboard Van Allen Probe A, and Figure 7c the total (the sum of electric and magnetic fields) empirical, *Kp*-driven D_{LL} radial diffusion coefficient, in units of days^{-1}, from *Ozeke et al.* [2014, equations 20 and 23]. On 13 November and most of 14 November, the IMF B_z baseline was slightly positive. After 16:00 UT on 14 November, the baseline went southward, leading to enhanced substorm activity. There is clear evidence in the tens to low hundreds of keV electrons of an injection just after 18:00 UT when the spacecraft was near apogee. Following that, through 16 November, the evidence of multiple energetic electron injections is clear. Moreover, the energetic electrons reach deeper and deeper into the magnetosphere, with those electrons being observed much farther from apogee as time goes on. The data from Van Allen Probe B (not shown) exhibit the same trend. The empirical D_{LL} diffusion coefficient also becomes larger in concert with the presence of southward IMF B_z baseline. At L shells larger than about 6, D_{LL} is on the order of 1 day^{-1}; thus, at those radial distances ULF wave-driven radial diffusion could be effective for increasing the flux of relativistic electrons in a timescale comparable to what is observed, i.e., around 1 day. These data, combined with the THEMIS data and simulation results, tell a compelling and consistent story.

The shift in the IMF baseline from northward to southward allowed for more extended periods of southward IMF that resulted in more extended southward IMF Dungey-cicle convection. This produced more substorm injections deeper into the magnetosphere; hence, keV electrons were able to penetrate deeper into the inner magnetosphere and provide an enhanced keV electron population that could be accelerated to MeV energies. However, in addition to a seed population one also needs a mechanism for accelerating that seed population, and, as we shall see, the shift in the IMF baseline from northward to southward had an impact on the accelerator, as did the increase in the solar wind speed on 16 November.

5. Global (BATS-R-US) Magnetosphere Runs and Magnetic Power Spectra Evaluation

In order to investigate the response of magnetic field power in the nightside, equatorial inner magnetosphere due to different fluctuating solar wind magnetic fields, a set of simplified global magnetospheric (MHD) runs were conducted with the Solar Wind Modeling Framework/BATS-R-US code [*Tóth et al.*, 2012] code, using the computational resources at NASA's Community Coordinated Modeling Center (CCMC, http://ccmc.gsfc.nasa.gov/index.php). The BATS-R-US code uses an adaptive, Cartesian grid whose spatial resolution increases by a factor of 2 as one approaches the Earth. The entire domain in our simulations was $-255 < x < 33$ and $-48 < y, z < -48$, where distances are measured in Earth radius (R_E) and the coordinate system used is GSM.

A higher-resolution grid of 0.125 R_E was used in the following domain $-7 < x, y < 7$ and $-3 < z < 3R_E$, and all simulations were performed with no dipole tilt inclination. In this way, we ensured that the radiation belts region in the simulation domain would be inside the higher-resolution grid region. Also, we did not use the Rice Convection Model [e.g., *De Zeeuw et al.*, 2004], since we wanted to rule out further complexities from the model, keeping the MHD runs as simple as possible.

At all simulations, the Pedersen conductivity was fixed at 10 mhos throughout the simulation period. All input parameters, with the exception of the IMF B_z component, were kept constant throughout the 6 h runs, and their values were such that we could have solar wind conditions resembling a high-speed stream. The solar wind inputs had temperature $T = 116,000$ K, corresponding to a solar wind sound speed of ~40 km/s, density $n = 3\ \mathrm{cm}^{-3}$, solar wind velocity $\mathbf{V} = -600$ km/s $\hat{\mathbf{x}}$, and IMF $B_x = B_y = 0$. The IMF B_z component was set to vary sinusoidally with time t, having the form

$$\mathrm{IMF}B_z(t) = B_{zo} + B_A \sin\left(2\pi \frac{t}{T_p}\right), \tag{1}$$

where B_A is the constant amplitude of the fluctuation, chosen to be $B_A = 2$ nT, and B_{zo} is the baseline value set to be either +0.5 nT, i.e., slightly northward B_z on average, or −0.5 nT, corresponding to a slightly southward IMF B_z on average. For both cases, the IMF B_z component fluctuates in both positive and negative domains, spending more time in the negative (positive) domain when the baseline value is negative (positive). A fluctuation period T_p of 20 min corresponding to a monochromatic oscillation frequency f_o of $f_o \approx 0.83$ mHz, has been chosen. Such fluctuation periods in the sub-mHz range as well as in the Pc5 (1.7 to 6.7 mHz) range have been shown to drive ULF wave activity in the inner magnetosphere, particularly at the geosynchronous orbit [see, e.g., *Kepko and Spence*, 2003, and references therein].

Due to our simplified solar wind input conditions where the IMF is set to vary only in one (z_{GSM}) direction, the inner magnetospheric magnetic field fluctuations in our simulations are mostly concentrated in the B_z component, which at the equator nearly corresponds to the direction of the local magnetic field vector. Thus, the magnetic field oscillations analyzed here are compressional in nature. According to Faraday's law these compressional oscillations are associated with azimuthal (in the equator plane)-induced electric field fluctuations, which in turn are believed to have the largest impact on azimuthally drifting radiation belt electrons [*Elkington et al.*, 2003; *Huang et al.*, 2010].

The simulations were evolved for 6 h of magnetospheric time. We then took only the last 2 h, i.e., from the 04:00:00 up to 06:00:00 time marks, to do a further analysis, since from this point (4 h mark) onward the simulated magnetosphere has reached a quasi-steady state. At each 30 s of magnetospheric time, a BATS-R-US output file was generated; thus, whichever time series obtained from the modeled parameters during this 2 h interval have 241 points, with a corresponding sampling rate f_s of $f_s = 1/30 \approx 33.3$ mHz, and a highest resolvable frequency, the Nyquist frequency $f_{\mathrm{Ny}} = f_s/2$, of 16.6 mHz.

5.1. Power Spectral Density on the Nightside Equatorial Plane: Role of IMF B_z Baseline and Solar Wind Speed

As mentioned above, from the three modeled magnetic field components B_x, B_y, and B_z, the fluctuations were mostly concentrated in the north-south B_z component; thus, from now on all results concerning the nightside, inner magnetosphere magnetic power spectral density (PSD) refer to those obtained by performing a Fourier spectral analysis in the time series of the modeled B_z component. We proceeded in the following way: at a given local time (LT), say 18:00 LT, and at a given radial distance R, a 2 h B_z time series is obtained for both

BATS-R-US runs, i.e., those with negative and positive IMF B_z baselines. Then, a Fourier analysis, as performed by *Claudepierre et al.* [2008], is done for each time series, and the PSDs are obtained in units of nT^2/Hz. Next, we integrate each PSD in the $[f_a, f_b]$ frequency band, where $f_a = 0.5$ mHz and $f_b = 16.6$ mHz, yielding what is called here integrated PSD (IPSD)

$$\mathrm{IPSD} = \int_{f_a}^{f_b} \mathrm{PSD(f)df} \quad \text{units of } (\mathrm{nT})^2. \tag{2}$$

Thus, we end up with representative values of the modeled magnetic wave power in the Pc4–5 frequency range for a given LT and a given radial distance R. In the next step, the radial distance R is incremented by an amount $dR = 0.065\ R_E$, while maintaining the same LT, and the process is repeated to reach until $R = 10\ R_E$. We start off at a radial distance $R = 3.5\ R_E$. Finally, we discretize the nightside, equatorial region into 100 equally sized LT bins starting at 18:00 LT and ending at 06:00 LT. We then obtain a map of IPSD values as a function of radial distance and LT. Such a map is shown in Figures 8a and 8b where they, respectively, correspond to IPSD values for negative, i.e., $B_{zo} = -0.5$ nT, and positive, $B_{zo} = +0.5$ nT, IMF B_z baselines, with both runs having the same input solar wind speed of 600 km/s. Figure 8c presents the ratio of $B_{zo} < 0$ over $B_{zo} > 0$ IPSD values with the same (600 km/s) input solar wind speed. For the nightside area plotted, ULF Pc4–5 IPSD values are in general higher when the magnetosphere is under the influence of a fluctuating IMF B_z with a slightly negative, on average, baseline. Figure 8c shows that IPSD values for a slightly negative, on average, IMF B_z baseline can be up to 55 times higher than those for slightly positive, on average, IMF B_z baselines. In most part, i.e., ~75% of the area in Figure 8c, IPSD values for a slightly negative baseline are at least 100% higher than those for a slightly positive baseline. Thus, we see that the overall effect of the shift in the IMF baseline from northward to southward was to increase the power in ULF fluctuations, just at the time that the seed population of keV electrons was increasing.

From around noon on 15 November up to the early morning hours of the 16th, the solar wind speed increased from around 500 km/s to above 600 km/s, while the IMF B_z baseline was slightly negative. During this period, the major refiling of the outer electron belt took place. We examine how such an increase in the solar wind speed impacts the magnetic fluctuation level on the nightside, equatorial inner magnetosphere as far as global MHD simulations are concerned. Previous works [e.g., *Claudepierre et al.*, 2008; *Huang et al.*, 2010] have shown that increasing solar wind speed in a global MHD simulation, while keeping constant all other input parameters, including the IMF, would increase both the magnetic field and the corresponding induced electric field fluctuation levels in the magnetosphere. We evaluate IPSD as a measure for the level of fluctuation in the magnetic field B_z component, as done above. We use a third BATS-R-US run where the solar wind speed is set at a constant value of 500 km/s, and the IMF B_z fluctuation has a negative ($B_{zo} = -0.5$ nT) baseline. All other input parameters are kept the same. We compare the IPSD values from this run with those from the previous 600 km/s, negative IMF B_z baseline run.

Figures 8d and 8e show IPSD values for input solar wind speeds of 600 km/s and 500 km/s, respectively, whereas Figure 8f the IPSD ratio, i.e., the $V_{sw} = 600$ km/s over the $V_{sw} = 500$ km/s IPSD values. An only 20% enhancement in the solar wind speed has lead to increases in the ULF Pc4–5 range IPSD values of at least 100% in about 90% of the colored area in Figure 8f. This provides us with an explanation for the large increase in the radiation belt flux on 16 November. The increase in the solar wind speed, along with an even greater seed population (compared to 15 November), may have contributed in the large flux increases of MeV electrons.

We note that in both cases analyzed, i.e., either by changing the IMF B_z baseline from slightly positive to slightly negative while keeping the input solar wind speed constant or by increasing the input solar wind speed while keeping the same slightly negative, on average, baseline, there were regions on the modeled nightside magnetosphere where the ULF Pc4–5 range IPSD values would decrease instead of increase. Such regions are not colored in both Figures 8c and 8f. We presently do not know why these uncolored regions have the spatial extent as shown in our simulations nor the reason they are there. Recall that we are employing oversimplified global MHD runs, and perhaps the coupling with inner magnetosphere modules should most likely better represent the physical processes occurring in such a region, providing a clue on whether the uncolored regions depicted in Figures 8c and 8f might in fact exist. We let such an investigation, however, to a future work. Nonetheless, our simulation results indicate that whenever the IMF B_z baseline is negative, particles being injected near the nightside inner edge of the plasma sheet (R ~8–10 R_E) will be subject, on its way to Earth, to higher levels of magnetic field fluctuations in the ULF Pc4–5 range up to radial distances

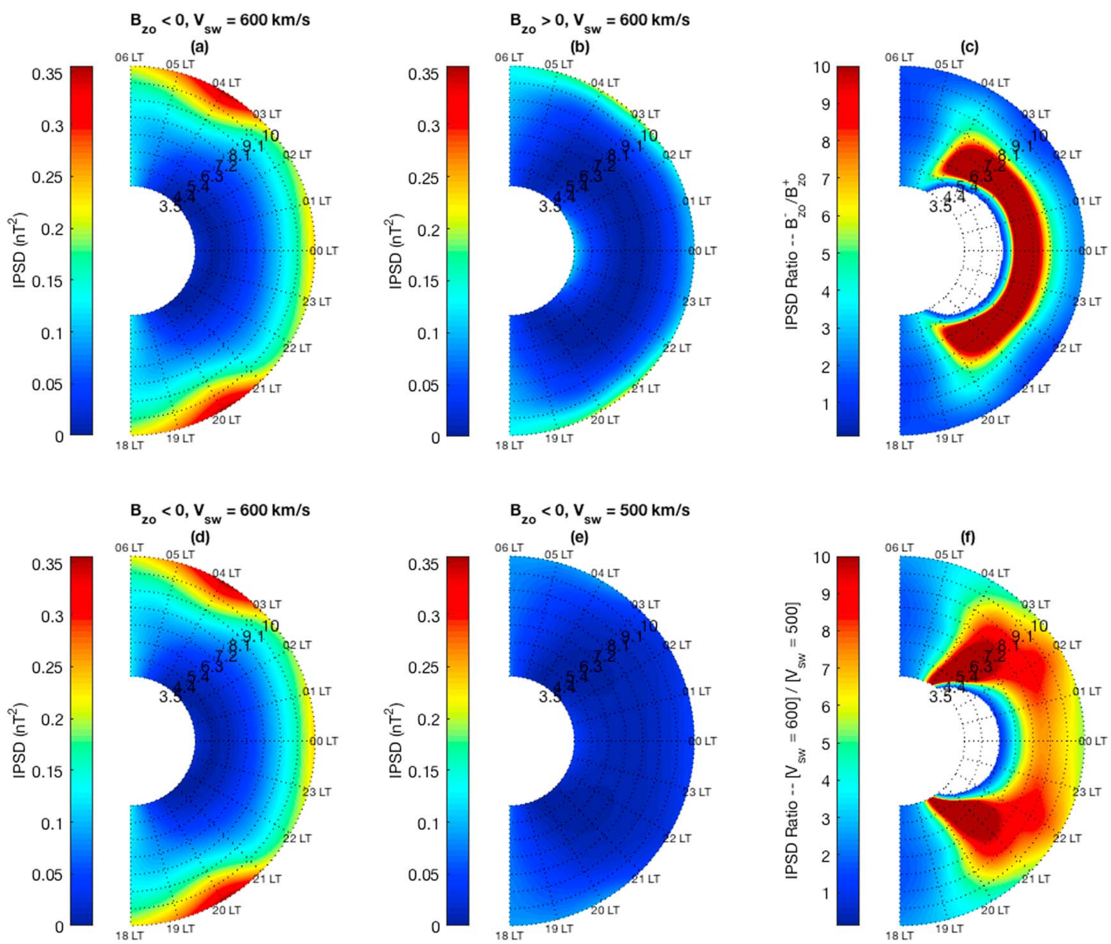

Figure 8. ULF Pc4–5 range-integrated power spectral density (IPSD) of the magnetospheric magnetic field component B_z in the BATS-R-US' nightside, equatorial region, as a function of radial distance (in Earth radii) and local time (LT). Radial distances vary from 3.5 to 10 R_E. (a, b) IPSD values obtained when the BATS-R-US code was run with a steady solar wind speed of 600 km/s and under a fluctuating IMF B_z component with slightly negative and positive, on average, baselines, respectively. The baseline values used were $B_{zo} = \pm 0.5$ nT. (c) The IPSD ratio, i.e., the ratio between IPSD values shown in Figure 8a over those in 8b. (d–f) The same format as Figures 8a–8c. Figure 8d is the same as Figure 8a, while Figure 8e presents IPSD values for a slightly, on average, negative baseline but with a solar wind speed of 500 km/s. Lastly, Figure 8f shows the ratio between IPSD values shown in Figure 8d over those in Figure 8e. Uncolored regions in Figures 8c and 8f denote places where the IPSD ratio is less than 1.

slightly lower ($\sim$5.5 R_E) than geosynchronous altitude. From this point, other wave-particle interaction mechanisms such as gyroresonant interactions mediated by whistler mode chorus waves might kick in and also play an important role on the electron acceleration. Indeed, we showed Van Allen Probes observations (Figure 3) of bursts of increased chorus wave activity. They occurred in concert with electron injections of tens to low hundreds of keV energies, with such injections being observed in situ by Van Allen Probe A.

Since both ULF and whistler mode chorus wave activities were enhanced when the IMF B_z baseline went southward, and also since electron's interaction with each of these two waves is inherently different, one might ask which acceleration mechanism leading to electron energies in the MeV range would be dominant, i.e., radial (ULF based) or local (chorus based) acceleration. One way to tackle this problem is by looking at time-dependent radial profiles of phase space densities (PhSDs) [see, e.g., *Green and Kivelson*, 2004; *Turner et al.*, 2012; *Reeves et al.*, 2013, and references therein]. The next section addresses this point.

6. Phase Space Density Analysis

When translating in situ particle flux measurements into phase space density (PhSD), it is appropriate to represent PhSD as a function of quantities which are conserved under specific circumstances like the three adiabatic invariants that constrain the electron motion: μ, K, and *Roederer*, 's [1970] L^* parameter (which is inversely proportional to the third adiabatic invariant; thus, it is also an invariant). Here we show time-dependent PhSD

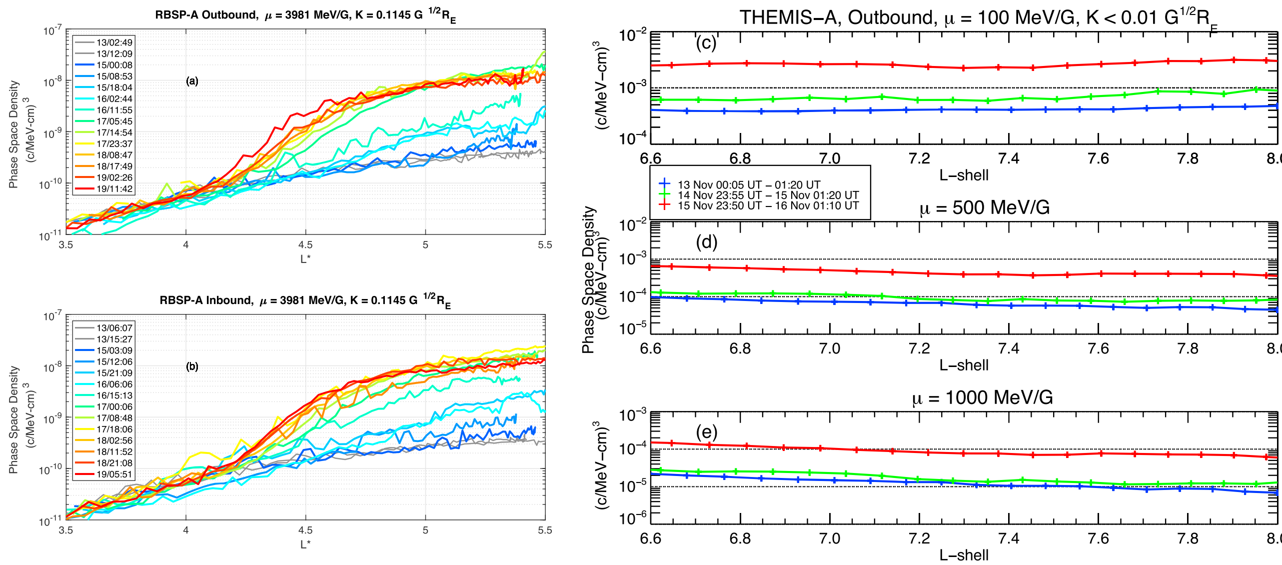

Figure 9. Time evolution of phase space density radial profiles at fixed first (μ) and second (K) adiabatic invariants for both (a) outbound and (b) inbound parts of the RBSP-A orbit path and (c–e) for the THEMIS A spacecraft during the outbound portion of its orbit. The second invariant value is the same for Figures 9c–9e, while the first adiabatic invariant is varied, covering electron energies as low as few hundreds of keV up to about 720 keV. The legends in Figures 9a and 9b show the start day and time (in the dd/hh:mm format) of either the outbound or inbound portions of RBSP-A. In contrast, legends in Figures 9c–9e present the whole time interval used to generate phase space density plots.

radial profiles, i.e., plots of PhSD as a function of L^* for fixed μ and K, at regions both within and beyond geosynchronous orbit. Figure 9 shows PhSD plots of both (a and b) Van Allen Probe A (RBSP-A) and (c–e) THEMIS A satellites for time periods encompassing the recovery of relativistic electron fluxes. PhSD data for RBSP-A were obtained directly from https://www.rbsp-ect.lanl.gov/data_pub/PSD/, where one can find PhSD data for a range of both μ and K values. For RBSP-A, values of $\mu = 3981$ MeV/G and $K = 0.1145$ G$^{1/2}$ R_E were used, since they optimized, for this case, the coverage in L^* while constraining the corresponding equatorial PhSD to approximately 45°–90° pitch angle range (see *Reeves et al.* [2013, supporting information] for more information). Furthermore, the higher μ value chosen corresponds to electrons at energies $\gtrsim$1.5 MeV at which the increase in the outer belt flux is observed. PhSD at THEMIS was obtained using the first 11 energy channels of the SST instrument, following the approach of *Turner et al.* [2012]. We note that we did not perform any intercalibration between data acquired by SST and REPT/MagEIS instruments; therefore, the absolute PhSD values obtained at both THEMIS A and RBSP-A locations cannot be directly compared, although the *signs* of PhSD gradients at these two locations can still be used for comparison, since they are not expected to change due to a lack of intercalibration. In what follows, we first present radial PhSD profiles obtained by THEMIS A followed by RBSP-A.

6.1. THEMIS

THEMIS A PhSD plots shown in Figures 9c–9e provide us with lower energy electron characteristics beyond geosynchronous orbit location. Since THEMIS is in a near-equatorial orbit, the value of the second adiabatic invariant is close to zero (< 0.01 G$^{1/2}$ R_E). Three values for the first adiabatic invariant were chosen, namely, $\mu =$ 100, 500, and 1000 MeV/G, so one can analyze the characteristics of particles with energies as low as several tens of keV up to about 720 keV. For lower energy (up to a few hundreds of keV) electrons, the gradient in PhSD, i.e., d PhSD/dL^*, is nearly flat with a slight positive increase as L^* becomes large, thus indicating a viable source of such low energy electrons at higher L^*. Also, the PhSD values are increasing as time progresses, consistent with THEMIS observations of lower energy (tens to low hundreds of keV) electron injections. For higher-energy electrons, however, the gradient changes sign from positive to negative, and thus, PhSD values decrease as the radial distance from geosynchronous increases. Such PhSD behavior for high-μ particles appears to be a common feature beyond geosynchronous orbit location, as reported by other studies [e.g., *Turner et al.*, 2012, and references therein].

Negative PhSD gradients beyond geosynchronous suggest that, for high-μ electrons, a peak in PhSD should exist inside geosynchronous, which in turn can be interpreted as evidence for local particle heating/acceleration as long as effects on the PhSD gradients due to (1) loss of particles at higher L^* and (2) time-dependent sources at higher L^* are negligible. The first of these scenarios indeed seems to play no role on the observed THEMIS A PhSD gradients, since according to *Turner et al.* [2012] loss of particles at higher L^* would generate negative PhSD gradients beyond geosynchronous orbit location regardless of the μ value. With regard to the second scenario, however, we cannot in principle rule it out, since THEMIS observations (Figure 5) show that lower energy electrons are constantly being injected in the plasma sheet region toward Earth, especially on 16 November where substorm activity reaches its peak. Therefore, time-dependent sources at higher L^* may be playing a role on the observed PhSD gradients.

6.2. Van Allen Probe (RBSP) A

When looking at the time evolution of PhSD radial profiles at both (Figure 9a) outbound and (Figure 9b) inbound portions of RBSP-A orbit, one can see that PhSD gradients are always positive, and there is no clear evidence of a localized peak in PhSD within the L^* range covered by this spacecraft, i.e., $3.5 \leq L^* \leq 5.5$. One can clearly see, however, that as time progresses PhSD initially starts increasing at higher L^* ($\gtrsim 5$), in concert with the southward turning of the IMF B_z baseline (which occurred at L1 location around 16:00 UT in 14 November), and then a more pronounced enhancement of PhSD values occurs for a higher range in L^*, reaching locations deep within the outer belt at $L^* \sim 4.5$. Nevertheless, as mentioned above, no clear peak developed as PhSD values continue to grow, as time goes by, at the outskirts of the outer belt, i.e., at $L^* \gtrsim 5$. We note that at lower μ values of up to $\sim$2200 MeV/G (while maintaining the same K) the absence of peaks in radial PhSD profiles persisted (not shown). This piece of evidence would tend to support the radial diffusion acceleration hypothesis as the main mechanism for accelerating outer belt electrons for this event. Nonetheless, the likelihood of a peak in PhSD being formed beyond RBSP-A's orbit apogee, especially around $L^* \gtrsim 5.5$ where the PhSD profile becomes nearly flat, cannot be discarded, particularly because negative PhSD gradients for up to 720 keV electrons beyond geosynchronous orbit location have been shown here via THEMIS observations throughout the analyzed period (13–16 November). In fact, peaks at $L^* \approx 5.5$ in PhSD for equatorially mirroring electrons have been reported elsewhere [see, e.g., *Chen et al.*, 2007, and references therein] as an indication of local acceleration as the dominant mechanism responsible for relativistic electron flux enhancements. When we analyze the time evolution of radial PhSD profiles at even lower μ values (in between $\sim$1318 and 1900 MeV/G) a peak in PhSD (not shown) appears to develop in the $L^* \sim$4.8–5 range but only on the late hours of 18 November onward. Prior to that, PhSD gradients were markedly positive at lower L^* values and nearly zero (flat PhSD profile) at higher L^*, consistent with a radial profile expected from ULF wave-driven radial diffusion.

7. Summary and Discussion

In this study we analyzed one of the possible scenarios leading to the relativistic outer belt electron flux recovery observed by the Van Allen Probes on the 13–16 November 2014 period, namely, (1) the arrival of a high-speed solar wind stream with the concurrent enhancement of nightside, hot (tens to few hundreds of keV energy) electron injections that occurred when the fluctuating IMF B_z component turned from slightly positive, on average, to slightly negative, on average, values and (2) the subsequent increase in both the nightside magnetic field integrated power spectral density in the ULF (0.5–16.6 mHz) band and the whistler mode chorus waves activity. In the following, we discuss each one of these scenarios separately.

Using magnetic field and plasma observations in the 14–16 November time frame from the THEMIS A spacecraft, conveniently located in the nightside, near-equatorial magnetosphere, we could identify a series of enhanced earthward plasma flows that occurred in concert with spatiotemporal magnetic field changes suggestive of dipolarization fronts [*Runov et al.*, 2009]. In the meantime, tens to few hundreds of keV energy electrons had their fluxes enhanced by nearly 1 order of magnitude. The occurrence of such electron injections systematically increased from the 14th up to the 16th, which correlates with the change in the IMF B_z's baseline, i.e., its 4 h running average value, from slightly positive to slightly negative. THEMIS observations suggest that injections occurring on both the 15th and 16th penetrate deeper into the inner magnetosphere than those on the 14th. The LFM simulation of the 14–16 November 2014 period seems to confirm this scenario. High-velocity flow channels reach locations slightly inside geosynchronous orbit on 16 November, according to our simulation result (see Figure 6). *Turner et al.* [2015] have recently shown that near-Earth plasma sheet injections triggered by substorm-associated dipolarizations, as those reported here, may indeed reach the inner magnetosphere. The implication is that hot electrons injected into the inner magnetosphere on the 15th and 16th, particularly on the latter day, could function as seed population in such a way that wave-particle interactions could take over and accelerate these electrons up to relativistic energies, as it has been proposed in the literature [*Baker et al.*, 1997; *Turner et al.*, 2014; *Jaynes et al.*, 2015; *Turner et al.*, 2015].

We also investigated the role played by the fluctuating IMF B_z component with both positive ($B_{zo} > 0$) and negative ($B_{zo} < 0$) baselines on the nightside, equatorial magnetosphere magnetic field fluctuation levels in the 0.5–16.6 mHz ULF band as probed by the integrated magnetic power spectral density (IPSD). We simulated the Earth's magnetospheric environment under solar wind conditions resembling those typically found at high-speed solar wind streams [see, e.g., *Tsurutani et al.*, 2006]. Since the synthetic solar wind magnetic field input used in this study is confined in the north-south (z GSM) direction, the magnetospheric magnetic field fluctuations were mostly concentrated in the B_z component, i.e., $\delta B_z \gg \delta B_x, \delta B_y$. Therefore, the ULF range magnetic field fluctuations analyzed here are essentially compressional in nature. Although not analyzed in this study, the induced azimuthal (in the equator plane) electric field fluctuations associated with the compressional magnetic field fluctuations via Faraday's law are believed to have the largest impact on azimuthally drifting radiation belt electrons [*Elkington et al.*, 2003; *Huang et al.*, 2010]. Our simplified global magnetosphere (BATS-R-US) simulation results showed that from slightly inside ($R \sim 5.5\,R_E$) of geosynchronous orbit and extending to radial distances of $\sim 10\,R_E$, regardless of local time, the IPSD values are always larger (at least 100% higher) when the solar wind driving has a slightly negative, on average, IMF B_z fluctuating component. When maintaining the negative baseline, but increasing the input solar wind speed from 500 to 600 km/s, as it was the case from midday on 15 November to the beginning of the 16th, even higher enhancements in the ULF band IPSD values were found, which is in accordance with previous works that used other magnetohydrodynamic (LFM) code [e.g., *Claudepierre et al.*, 2008; *Huang et al.*, 2010]. In this respect, our simulation results for higher nightside, equatorial IPSD values for higher solar wind speeds are also in agreement with previous observational works that used both ground-based and space-based magnetometer data [see *Pokhotelov et al.*, 2015, and references therein]. Van Allen Probes observations indeed showed a gradual increase in the magnetic field power spectral densities in the 0.5 to 16 mHz range from 13 to 16 November, with a particularly enhanced activity on both the 15th and 16th (see Figure 2). By using the analytical expression of an empirical, *Kp* index-driven radial diffusion coefficient [*Ozeke et al.*, 2014], it was found that at L shells larger than about $L = 6$, ULF wave-driven radial diffusion could be effective for increasing the flux of relativistic electrons in a timescale comparable to what was observed, i.e., around 1 day.

We notice that during the analyzed relativistic electron flux recovery period the whistler mode chorus wave activity was gradually increasing as detected by both Van Allen Probes. On 14 November there was a moderate enhancement in the magnetic field power spectral density as compared to the 13th, but it was on the 15th that intensified chorus wave activity was present during the whole day. This scenario persisted throughout the 16th, and the intensified chorus wave activity subsided at ∼06:00 UT on the 17th. Occasional bursts of intensified activity occurred afterward, but they were not as intense. Therefore, it is also likely that chorus waves could be playing an important role on the electron flux recovery event studied here [see *Miyoshi et al.*, 2013].

We presented time-dependent radial profiles of phase space density (PhSD) both within and beyond geosynchronous orbit location in order to have a clue on which mechanism, i.e., ULF wave-driven radial diffusion or chorus wave-driven local acceleration, would be the dominant for the observed recovery in the relativistic electron flux. Regarding the analysis of PhSD within geosynchronous orbit location, our results showed that in spite of the presence, along most part of Van Allen Probe A orbits, of bursts of increased chorus wave activity there were no clear evidences of peaks in PhSD, at least not in the $3.5 \leq L^* \leq 5.5$ range covered by RBSP-A and for the analyzed first (μ) and second (K) adiabatic invariant values of 3981 MeV/G and 0.1145 $G^{1/2}\,R_E$, respectively. Such high μ value corresponds to electron energies of $\gtrsim$1.5 MeV at which the recovery of the relativistic electron flux is observed. We note that at lower μ values of up to ∼2200 MeV/G (while maintaining the same K) the absence of peaks in radial PhSD profiles persisted (not shown), and these profiles were very similar to those shown in Figures 9a and 9b. At even lower μ ($\lesssim$1900 MeV/G) values, however, particularly for $\mu = 1318$ MeV/G, a peak in PhSD (not shown) appears to develop in the L^* ∼4.8–5 range but only on the late hours of 18 November onward. Prior to that, PhSD gradients were markedly positive at lower L^* (4.3–4.6) values and nearly zero (flat PhSD profile) at higher L^* ($\gtrsim$ 5.2) consistent with a radial profile expected from ULF wave-driven radial diffusion. With regard to radial PhSD profiles beyond geosynchronous orbit, as derived from particle flux measurements aboard the THEMIS A spacecraft, two main features can be highlighted: the first one is that, as time progresses, PhSD values increase at all radial positions covered by the spacecraft regardless of the analyzed μ values of 100, 500, and 1000 MeV/G; the second main feature is that PhSD radial gradients, i.e., $d\,\mathrm{PhSD}/dL^*$, are μ dependent with the gradient changing sign from positive to negative as the μ value increases. Such a feature has been found previously in the literature [e.g., *Turner et al.*, 2012]. For lower energy ($\mu = 100$ MeV/G) electrons both the positive sign of the PhSD gradient and the increase in PhSD values as time goes by are consistent with both a viable and increasing (in flux) source of lower (tens to low hundreds of keV) energy electrons being injected farther out from the THEMIS A location. Such lower energy electrons were indeed observed by THEMIS A throughout the analyzed period (14 to 16 November). The negative gradient sign observed for higher-energy ($\mu \geq 500$ MeV/G) electrons indicate that a peak in PhSD should exist within geosynchronous. As just mentioned above, indication that such a peak is present within geosynchronous orbit occurs only for electron energies below 1 MeV on the late hours of 18 November onward, when the relativistic electron flux had already recovered to prestorm levels.

Based on the PhSD analysis presented so far, our interpretation is that, for this relativistic electron flux recovery event, the time evolution of radial PhSD profiles does not provide a conclusive evidence on which electron acceleration mechanism, i.e., radial diffusion or local acceleration, is the dominant one. On the one hand, while the presence of enhanced whistler mode chorus waves activity along the Van Allen Probes orbits favors the idea that local acceleration should be occurring [see, e.g., *Thorne et al.*, 2013], no clear peaks in the PhSD are observed within geosynchronous orbit location at least for the analyzed values of the first (~2200–3981 MeV/G) and second (0.1145 $G^{1/2}\,R_E$) adiabatic invariants. We are by no means saying that local chorus wave-driven acceleration is not occurring but only emphasizing that its effect on the time evolution of PhSD radial profiles is not evident. Instead, radial PhSD profiles characteristic of radial diffusion developed during the course of the electron acceleration event. On the other hand, we have negative PhSD gradients, for electron energies lower than about 720 keV, observed beyond geosynchronous orbit which suggest that a PhSD peak should exist within geosynchronous, which in turn might be an indicative of local acceleration via gyroresonant interactions with very low frequency range waves [see, e.g., *Chen et al.*, 2007]. One thing is clear though: the inner magnetosphere dynamics, as analyzed by the dynamical behavior of the relativistic electron flux in the outer radiation belt, showed significant changes when a slightly southward IMF B_z baseline along with an increased solar wind speed impinged on the Earth's magnetosphere, enabling (i) an enhancement in the whistler mode chorus wave activity, (ii) an intense substorm activity which in turn provided the seed population that is subsequently accelerated to MeV energies, and (iii) a substantial, higher than 100% increase in wave power in the ULF Pc4–5 frequency range.

Our study using both in situ observations and global magnetosphere simulations suggests that the IMF B_z baseline turning from a slightly, on average, positive (northward) to a slightly negative (southward) orientation on the late hours of 14 November, and more importantly the persistence of this state up to the end of the 16th along with an increase in the solar wind speed characteristic of a high-speed stream, engendered an enhanced occurrence of nightside, hot electron injections. In this period, the ULF range magnetic field compressional (and most likely the azimuthal electric field) fluctuations were higher, as far as global MHD simulations and the Van Allen Probes observations are concerned, which in turn would increase the effectiveness of drift-resonant interactions mediated by ULF range waves with either nightside injected or preexisting radiation belt electrons. Also, the detection of intensified chorus waves activity in the entirety of the outer electron belt during the analyzed period suggests that in addition to ULF wave-driven radial diffusion, chorus wave-driven local acceleration could also be playing an important role on the recovery of the relativistic electron flux. However, our interpretation of the observations presented here do not allow us to decisively say which of two mechanisms is the dominant one. Both of them appear to be playing an important role. The main point we would like to stress is the major changes in the outer radiation belt fluxes when the solar wind driver changed so little, i.e., an only 20% increase in solar wind speed in conjunction with a southward turning of a small (within ±4 nT) IMF B_z baseline.

Acknowledgments
This research was partially funded by the São Paulo Research Foundation (FAPESP) grants 2014/21229-9 and 2015/20104-0. P.R. Jauer thanks the Brazilian National Council for Research and Development (CNPq) via the PCI grant 313281/2015-7 for the financial support. D. Koga thanks CNPq grant 112886/2015-9. This work was also supported by NASA grant NNX15AJ03G. Work at GSFC was supported by the Van Allen Probes mission. Van Allen Probes and THEMIS data are freely available at https://rbsp-ect.lanl.gov/science/DataDirectories.php and http://themis.ssl.berkeley.edu/software.shtml, respectively. Data at the L1 Lagrangian point provided by the ACE spacecraft can be readily found at http://www.srl.caltech.edu/ACE/ASC/level2/index.html. This work was carried out using the SWMF/BATS-R-US tools developed at the University of Michigan's Center for Space Environment Modeling (CSEM) and made available through the NASA Community Coordinated Modeling Center (CCMC). We also acknowledge support from the APS/SBF Brazil-U.S. Professorship/Lectureship Program.

References

Angelopoulos, V., W. Baumjohann, C. F. Kennel, F. V. Coroniti, M. G. Kivelson, R. Pellat, R. J. Walker, H. Lühr, and G. Paschmann (1992), Bursty bulk flows in the inner central plasma sheet, *J. Geophys. Res.*, *97*(A4), 4027–4039, doi:10.1029/91JA02701.
Angelopoulos, V., et al. (2008), First results from the THEMIS mission, *Space Sci. Rev.*, *141*(1), 453–476, doi:10.1007/s11214-008-9378-4.
Auster, H. U., et al. (2009), The themis fluxgate magnetometer, in *The THEMIS Mission*, edited by J. L. Burch and V. Angelopoulos, pp. 235–264, Springer, New York, doi:10.1007/978-0-387-89820-9_11.

Baker, D. N., et al. (1997), Recurrent geomagnetic storms and relativistic electron enhancements in the outer magnetosphere: ISTP coordinated measurements, *J. Geophys. Res.*, *102*(A7), 14,141–14,148, doi:10.1029/97JA00565.

Baker, D. N., et al. (1998), A strong CME-related magnetic cloud interaction with the Earth's magnetosphere: ISTP observations of rapid relativistic electron acceleration on May 15, 1997, *Geophys. Res. Lett.*, *25*(15), 2975–2978, doi:10.1029/98GL01134.

Baker, D. N., et al. (2013), The relativistic electron-proton telescope (REPT) instrument on board the radiation belt storm probes (RBSP) spacecraft: Characterization of Earth's radiation belt high-energy particle populations, *Space Sci. Rev.*, *179*(1–4), 337–381.

Blake, J. B., D. N. Baker, N. Turner, K. W. Ogilvie, and R. P. Lepping (1997), Correlation of changes in the outer-zone relativistic-electron population with upstream solar wind and magnetic field measurements, *Geophys. Res. Lett.*, *24*(8), 927–929, doi:10.1029/97GL00859.

Blake, J. B., et al. (2013), The magnetic electron ion spectrometer (MagEIS) instruments aboard the radiation belt storm probes (RBSP) spacecraft, *Space Sci. Rev.*, *179*(1), 383–421, doi:10.1007/s11214-013-9991-8.

Chen, Y., G. D. Reeves, and R. H. W. Friedel (2007), The energization of relativistic electrons in the outer Van Allen radiation belt, *Nat. Phys.*, *3*(9), 614–617.

Claudepierre, S. G., S. R. Elkington, and M. Wiltberger (2008), Solar wind driving of magnetospheric ulf waves: Pulsations driven by velocity shear at the magnetopause, *J. Geophys. Res.*, *113*, A05218, doi:10.1029/2007JA012890.

De Zeeuw, D. L., S. Sazykin, R. A. Wolf, T. I. Gombosi, A. J. Ridley, and G. Tóth (2004), Coupling of a global MHD code and an inner magnetospheric model: Initial results, *J. Geophys. Res.*, *109*, A12219, doi:10.1029/2003JA010366.

Elkington, S. R., M. K. Hudson, and A. A. Chan (1999), Acceleration of relativistic electrons via drift-resonant interaction with toroidal-mode pc-5 ulf oscillations , *Geophys. Res. Lett.*, *26*(21), 3273–3276, doi:10.1029/1999GL003659.

Elkington, S. R., M. K. Hudson, and A. A. Chan (2003), Resonant acceleration and diffusion of outer zone electrons in an asymmetric geomagnetic field, *J. Geophys. Res.*, *108*(A3), 1116, doi:10.1029/2001JA009202.

Gonzalez, W. D., F. L. Guarnieri, A. L. Clua-Gonzalez, E. Echer, M. V. Alves, T. Ogino, and B. T. Tsurutani (2006), Magnetospheric energetics during HILDCAAs, in *Recurrent Magnetic Storms: Corotating Solar Wind Streams*, edited by B. T. Tsurutani et al., chap. 13, pp. 175–182, AGU, Washington, D. C.

Green, J. C., and M. G. Kivelson (2004), Relativistic electrons in the outer radiation belt: Differentiating between acceleration mechanisms, *J. Geophys. Res.*, *109*, A03213, doi:10.1029/2003JA010153.

Hietala, H., E. K. J. Kilpua, D. L. Turner, and V. Angelopoulos (2014), Depleting effects of ICME-driven sheath regions on the outer electron radiation belt, *Geophys. Res. Lett.*, *41*, 2258–2265, doi:10.1002/2014GL059551.

Horne, R. B., N. P. Meredith, R. M. Thorne, D. Heynderickx, R. H. A. Iles, and R. R. Anderson (2003a), Evolution of energetic electron pitch angle distributions during storm time electron acceleration to megaelectronvolt energies, *J. Geophys. Res.*, *108*(A1), 1016, doi:10.1029/2001JA009165.

Horne, R. B., S. A. Glauert, and R. M. Thorne (2003b), Resonant diffusion of radiation belt electrons by whistler-mode chorus, *Geophys. Res. Lett.*, *30*(9), 1493, doi:10.1029/2003GL016963.

Horne, R. B., M. M. Lam, and J. C. Green (2009), Energetic electron precipitation from the outer radiation belt during geomagnetic storms, *Geophys. Res. Lett.*, *36*, L19104, doi:10.1029/2009GL040236.

Huang, C.-L., H. E. Spence, H. J. Singer, and W. J. Hughes (2010), Modeling radiation belt radial diffusion in ULF wave fields: 1. Quantifying ULF wave power at geosynchronous orbit in observations and in global MHD model, *J. Geophys. Res.*, *115*, A06215, doi:10.1029/2009JA014917.

Jaynes, A. N., et al. (2015), Source and seed populations for relativistic electrons: Their roles in radiation belt changes, *J. Geophys. Res. Space Physics*, *120*, 7240–7254, doi:10.1002/2015JA021234.

Kataoka, R., and Y. Miyoshi (2006), Flux enhancement of radiation belt electrons during geomagnetic storms driven by coronal mass ejections and corotating interaction regions, *Space Weather*, *4*, S09004, doi:10.1029/2005SW000211.

Kepko, L., and H. E. Spence (2003), Observations of discrete, global magnetospheric oscillations directly driven by solar wind density variations, *J. Geophys. Res.*, *108*(A6), 1257, doi:10.1029/2002JA009676.

Kilpua, E., H. Hietala, D. Turner, H. Koskinen, T. Pulkkinen, J. Rodriguez, G. Reeves, S. Claudepierre, and H. Spence (2015), Unraveling the drivers of the storm time radiation belt response, *Geophys. Res. Lett.*, *42*, 3076–3084, doi:10.1002/2015GL063542.

Kim, H.-J., A. A. Chan, R. A. Wolf, and J. Birn (2000), Can substorms produce relativistic outer belt electrons?, *J. Geophys. Res.*, *105*(A4), 7721–7735, doi:10.1029/1999JA900465.

Kletzing, C., et al. (2013), The electric and magnetic field instrument suite and integrated science (EMFISIS) on RBSP, *Space Sci. Rev.*, *179*(1–4), 127–181.

Li, W., et al. (2014), Radiation belt electron acceleration by chorus waves during the 17 March 2013 storm, *J. Geophys. Res. Space Physics*, *119*, 4681–4693, doi:10.1002/2014JA019945.

Lopez, R., S. Bhattarai, R. Bruntz, K. Pham, M. Wiltberger, J. Lyon, Y. Deng, and Y. Huang (2012), The role of dayside merging in generating the ionospheric potential during the whole heliospheric interval, *J. Atmos. Sol. Terr. Phys.*, *83*, 63–69, doi:10.1016/j.jastp.2012.03.001. corotating Interaction Regions from Sun to Earth: Modeling their formation, evolution and geoeffectiveness.

Lopez, R. E., C. C. Goodrich, G. D. Reeves, R. D. Belian, and A. Taktakishvili (1994), Midtail plasma flows and the relationship to near-Earth substorm activity: A case study, *J. Geophys. Res.*, *99*(A12), 23,561–23,569, doi:10.1029/94JA01771.

Lopez, R. E., C. C. Goodrich, M. Wiltberger, K. Papadopoulos, and J. G. Lyon (1998), Simulation of the March 9, 1995 substorm and initial comparison to data, in *Geospace Mass and Energy Flow*, edited by J. L. Horwitz, D. L. Gallagher, and W. K. Peterson, pp. 237–245, AGU, Washington, D. C.

Lopez, R. E., J. G. Lyon, E. Mitchell, R. Bruntz, V. G. Merkin, S. Brogl, F. Toffoletto, and M. Wiltberger (2009), Why doesn't the ring current injection rate saturate?, *J. Geophys. Res.*, *114*, A02204, doi:10.1029/2008JA013141.

Lopez, R. E., R. Bruntz, E. J. Mitchell, M. Wiltberger, J. G. Lyon, and V. G. Merkin (2010), Role of magnetosheath force balance in regulating the dayside reconnection potential, *J. Geophys. Res.*, *115*, A12216, doi:10.1029/2009JA014597.

Lyon, J., J. Fedder, and C. Mobarry (2004), The Lyon–Fedder–Mobarry (LFM) global {MHD} magnetospheric simulation code, *J. Atmos. Sol. Terr. Phys.*, *66*(15–16), 1333–1350, doi:10.1016/j.jastp.2004.03.020. towards an Integrated Model of the Space Weather System.

Mauk, B., N. Fox, S. Kanekal, R. Kessel, D. Sibeck, and A. Ukhorskiy (2013), Science objectives and rationale for the radiation belt storm probes mission, *Space Sci. Rev.*, *179*(1–4), 3–27.

McFadden, J. P., C. W. Carlson, D. Larson, M. Ludlam, R. Abiad, B. Elliott, P. Turin, M. Marckwordt, and V. Angelopoulos (2009), The THEMIS ESA plasma instrument and in-flight calibration, in *The THEMIS Mission*, edited by J. L. Burch and V. Angelopoulos, pp. 277–302, Springer, New York, doi:10.1007/978-0-387-89820-9_13.

McIlwain, C. E. (1961), Coordinates for mapping the distribution of magnetically trapped particles, *J. Geophys. Res.*, *66*(11), 3681–3691, doi:10.1029/JZ066i011p03681.

Meredith, N. P., R. B. Horne, M. M. Lam, M. H. Denton, J. E. Borovsky, and J. C. Green (2011), Energetic electron precipitation during high-speed solar wind stream driven storms, *J. Geophys. Res.*, *116*, A05223, doi:10.1029/2010JA016293.

Miyoshi, Y., and R. Kataoka (2008), Flux enhancement of the outer radiation belt electrons after the arrival of stream interaction regions, *J. Geophys. Res.*, *113*, A03S09, doi:10.1029/2007JA012506.

Miyoshi, Y., R. Kataoka, Y. Kasahara, A. Kumamoto, T. Nagai, and M. F. Thomsen (2013), High-speed solar wind with southward interplanetary magnetic field causes relativistic electron flux enhancement of the outer radiation belt via enhanced condition of whistler waves, *Geophys. Res. Lett.*, *40*, 4520–4525, doi:10.1002/grl.50916.

O'Brien, T. P., K. R. Lorentzen, I. R. Mann, N. P. Meredith, J. B. Blake, J. F. Fennell, M. D. Looper, D. K. Milling, and R. R. Anderson (2003), Energization of relativistic electrons in the presence of ULF power and MeV microbursts: Evidence for dual ULF and VLF acceleration, *J. Geophys. Res.*, *108*(A8), 1329, doi:10.1029/2002JA009784.

Ozeke, L. G., I. R. Mann, K. R. Murphy, I. Jonathan Rae, and D. K. Milling (2014), Analytic expressions for ULF wave radiation belt radial diffusion coefficients, *J. Geophys. Res. Space Physics*, *119*, 1587–1605, doi:10.1002/2013JA019204.

Papadopoulos, K., C. Goodrichl, M. Wiltberger, R. Lopez, and J. Lyon (1999), The physics of substorms as revealed by the ISTP, *Phys. Chem. Earth Part C*, *24*(1–3), 189–202, doi:10.1016/S1464-1917(98)00028-2. international Symposium on Solar-Terrestrial Coupling Processes.

Pokhotelov, D., I. J. Rae, K. R. Murphy, and I. R. Mann (2015), The influence of solar wind variability on magnetospheric ULF wave power, *Ann. Geophys.*, *33*(6), 697–701.

Reeves, G. D., D. N. Baker, R. D. Belian, J. B. Blake, T. E. Cayton, J. F. Fennell, R. H. W. Friedel, M. M. Meier, R. S. Selesnick, and H. E. Spence (1998), The global response of relativistic radiation belt electrons to the January 1997 magnetic cloud, *Geophys. Res. Lett.*, *25*(17), 3265–3268, doi:10.1029/98GL02509.

Reeves, G. D., K. L. McAdams, R. H. W. Friedel, and T. P. O'Brien (2003), Acceleration and loss of relativistic electrons during geomagnetic storms, *Geophys. Res. Lett.*, *30*(10), 1529, doi:10.1029/2002GL016513.

Reeves, G. D., et al. (2013), Electron acceleration in the heart of the Van Allen radiation belts, *Science*, *341*(6149), 991–994.

Roederer, J. G. (1970), *Dynamics of Geomagnetically Trapped Radiation*, Springer, Berlin.

Rostoker, G., S. Skone, and D. N. Baker (1998), On the origin of relativistic electrons in the magnetosphere associated with some geomagnetic storms, *Geophys. Res. Lett.*, *25*(19), 3701–3704, doi:10.1029/98GL02801.

Runov, A., V. Angelopoulos, M. I. Sitnov, V. A. Sergeev, J. Bonnell, J. P. McFadden, D. Larson, K.-H. Glassmeier, and U. Auster (2009), THEMIS observations of an earthward-propagating dipolarization front, *Geophys. Res. Lett.*, *36*, L14106, doi:10.1029/2009GL038980.

Thorne, R. M., et al. (2013), Rapid local acceleration of relativistic radiation-belt electrons by magnetospheric chorus, *Nature*, *504*(7480), 411–414.

Tóth, G., et al. (2012), Adaptive numerical algorithms in space weather modeling, *J. Comput. Phys.*, *231*(3), 870–903.

Tsurutani, B. T., et al. (2006), Corotating solar wind streams and recurrent geomagnetic activity: A review, *J. Geophys. Res.*, *111*, A07S01, doi:10.1029/2005JA011273.

Turner, D. L., V. Angelopoulos, Y. Shprits, A. Kellerman, P. Cruce, and D. Larson (2012), Radial distributions of equatorial phase space density for outer radiation belt electrons, *Geophys. Res. Lett.*, *39*, L09101, doi:10.1029/2012GL051722.

Turner, D. L., et al. (2014), Competing source and loss mechanisms due to wave-particle interactions in Earth's outer radiation belt during the 30 September to 3 October 2012 geomagnetic storm, *J. Geophys. Res. Space Physics*, *119*, 1960–1979, doi:10.1002/2014JA019770.

Turner, D. L., et al. (2015), Energetic electron injections deep into the inner magnetosphere associated with substorm activity, *Geophys. Res. Lett.*, *42*, 2079–2087, doi:10.1002/2015GL063225.

Wiltberger, M., T. I. Pulkkinen, J. G. Lyon, and C. C. Goodrich (2000), MHD simulation of the magnetotail during the December 10, 1996, substorm, *J. Geophys. Res.*, *105*(A12), 27,649–27,663, doi:10.1029/1999JA000251.

Wiltberger, M., L. Qian, C.-L. Huang, W. Wang, R. E. Lopez, A. G. Burns, S. C. Solomon, Y. Deng, and Y. Huang (2012), {CMIT} study of CR2060 and 2068 comparing {L1} and {MAS} solar wind drivers, *J. Atmos. Sol. Terr. Phys.*, *83*, 39–50, doi:10.1016/j.jastp.2012.01.005, Corotating interaction regions from Sun to Earth: Modeling their formation, evolution and geoeffectiveness.

Wrenn, G. L., and R. J. K. Smith (1996), The ESD threat to GEO satellites: Empirical models for observed effects due to both surface and internal charging, in *Environment Modeling for Space-Based Applications, ESA Spec. Publ.*, vol. 392, edited by T.-D. Guyenne and A. Hilgers, pp. 121–124, ESA, Noordwijk, Netherlands.